THE JOURNAL OF PHYSICAL CHEMISTRY C
A JOURNAL OF THE AMERICAN CHEMICAL SOCIETY

pubs.acs.org/JPCC

Article

Relationships between Compositional Heterogeneity and Electronic Spectra of $(Ga_{1-x}Zn_x)(N_{1-x}O_x)$ Nanocrystals Revealed by Valence Electron Energy Loss Spectroscopy

Published as part of The Journal of Physical Chemistry C virtual special issue "Honoring Michael R. Berman".

Benjamin F. Hammel,[‖] Leah M. G. Hall,[‖] Lauren M. Pellows, Orion M. Pearce, Pornthip Tongying, Sadegh Yazdi, and Gordana Dukovic*

Cite This: *J. Phys. Chem. C* 2023, 127, 7762−7771

Read Online

ACCESS | Metrics & More | Article Recommendations | Supporting Information

ABSTRACT: Many ternary and quaternary semiconductors have been made in nanocrystalline forms for a variety of applications, but we have little understanding of how well their ensemble properties reflect the properties of individual nanocrystals. We examine electronic structure heterogeneities in nanocrystals of $(Ga_{1-x}Zn_x)(N_{1-x}O_x)$, a semiconductor that splits water under visible illumination. We use valence electron energy loss spectroscopy (VEELS) in a scanning transmission electron microscope to map out electronic spectra of $(Ga_{1-x}Zn_x)(N_{1-x}O_x)$ nanocrystals with a spatial resolution of 8 nm. We examine three samples with varying degrees of intraparticle and interparticle compositional heterogeneity and ensemble optical spectra that range from a single band gap in the visible to two band gaps, one in the visible and one in the UV. The VEELS spectra resemble the ensemble absorption spectra for a sample with a homogeneous elemental distribution and a single band gap and, more interestingly, one with intraparticle compositional heterogeneity and two band gaps. We observe spatial variation in VEELS spectra only with significant interparticle compositional heterogeneity. Hence, we reveal the conditions under which the ensemble spectra reveal the optical properties of individual $(Ga_{1-x}Zn_x)(N_{1-x}O_x)$ particles. More broadly, we illustrate how VEELS can be used to probe electronic heterogeneities in compositionally complex nanoscale semiconductors.

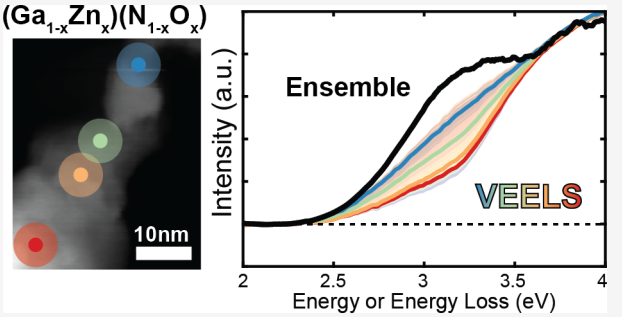

INTRODUCTION

$(Ga_{1-x}Zn_x)(N_{1-x}O_x)$ is a quaternary semiconductor with unusual optical properties: although the parent semiconductors, GaN and ZnO, have UV band gaps, $(Ga_{1-x}Zn_x)(N_{1-x}O_x)$ absorbs in the visible, in an apparent violation of Vegard's law, with the band gap determined by the value of x.[1−6] The absorption of visible wavelengths of sunlight and chemical stability have led to interest in using $(Ga_{1-x}Zn_x)(N_{1-x}O_x)$ for photochemical water splitting[1,2,6,7] and, more recently, Z-scheme CO_2 reduction[8] and photobiocatalytic H_2 evolution.[9] The origin of visible absorption in $(Ga_{1-x}Zn_x)(N_{1-x}O_x)$ remains under debate, with leading candidates being p−d repulsion between N 2p and Zn 3d atomic orbitals that increases the valence band energy,[3,10−12] the formation of defect bands,[13] and interfacial absorption between small domains of ZnO and GaN.[6]

In nanocrystalline form, $(Ga_{1-x}Zn_x)(N_{1-x}O_x)$ exhibits compositional complexity that is a direct consequence of the nanoscale solid state transformations used for its synthesis. Nanocrystals (NCs) of $(Ga_{1-x}Zn_x)(N_{1-x}O_x)$ can be made single-crystalline over a wide range of x values via solid state conversion of nanocrystalline starting materials $ZnGaO_4$ and ZnO under NH_3 flow.[14,15] At lower synthesis temperatures (650 °C), the resulting materials have ensemble compositions ranging from x = 0.06 to 0.98 and composition-dependent band gap energies in the visible region ranging from 2.25 to 2.9 eV.[15] (Bulk $(Ga_{1-x}Zn_x)(N_{1-x}O_x)$ synthesis requires higher temperatures that lead to Zn evaporation and limit the range of available x values.[2,16]) In the composition range of x = 0.06 to 0.66, the ensemble absorption spectra reflect a single visible band gap, while at high values of x, the spectra reflect the presence of both a visible, composition-dependent band gap and a UV band gap at ∼3.2 eV.[15] Energy-dispersive X-ray spectroscopy (EDS) in scanning transmission electron

Received: January 25, 2023
Revised: March 20, 2023
Published: April 17, 2023

microscopy (STEM) has revealed that this "low-temperature" synthesis leads to significant spatial compositional heterogeneity, including the presence of core−shell-like particles with Zn-rich cores and Ga-rich shells (Figure 1, top).[17] This

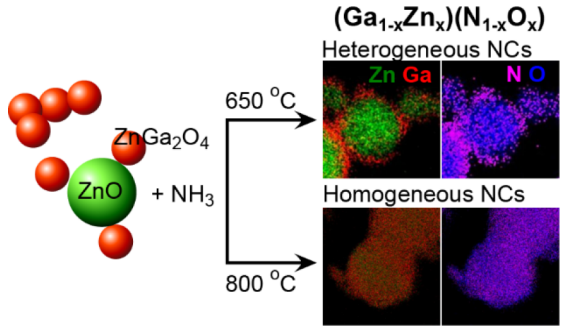

Figure 1. Relationship between the synthesis temperature and the elemental distribution in $(Ga_{1-x}Zn_x)(N_{1-x}O_x)$ NCs, as determined by STEM-EDS mapping. Adapted with permission from ref 17. Copyright 2017 American Chemical Society.

compositional heterogeneity is thought to originate from the incomplete diffusion of Ga and N during the solid state transformation.[17] In contrast, "high-temperature" (800 °C) syntheses lead to $(Ga_{1-x}Zn_x)(N_{1-x}O_x)$ NCs with homogeneous elemental distribution, where the composition of individual particles matches that of the ensemble sample and the four elements Ga, Zn, N, and O are evenly distributed around the particle (Figure 1, bottom).[17] These compositionally homogeneous particles also have composition-dependent band gaps in the visible region, with a single visible band gap seen in the absorption spectra.[17] Due to Zn evaporation, high x values have not been reported for the high-temperature synthesis, and the reported composition range is x = 0.11 to 0.44.[17]

The synthetically controlled elemental distribution observed in $(Ga_{1-x}Zn_x)(N_{1-x}O_x)$ NCs raises important questions about the relationships between the local elemental distribution and the local electronic structure. Specifically, it is not known to what extent the optical properties of the ensemble samples reflect those of the individual particles and how much the absorption spectra of individual particles vary across an ensemble sample. For example, for the compositionally heterogeneous high-x-value $(Ga_{1-x}Zn_x)(N_{1-x}O_x)$ nanocrystals synthesized at 650 °C, do the two band gap values observed in the ensemble spectra correspond to two different types of particles or do they correspond to two band gaps in each particle? Revealing the relationships between local composition and local electronic structure is essential to understanding the optical properties of compositionally complex nanomaterials.[18] It is also essential for applications that rely on these optical properties, such as the solar photochemistry of $(Ga_{1-x}Zn_x)(N_{1-x}O_x)$, where it is critically important to use materials with absorption spectra that significantly overlap with the solar irradiation spectrum.[19−22]

In this article, we address the relationships between the elemental distribution and electronic structure in $(Ga_{1-x}Zn_x)(N_{1-x}O_x)$ NCs using valence electron energy loss spectroscopy in scanning transmission electron microscopy mode (STEM-VEELS), which measures local electronic spectra with high spatial resolution. We analyzed three samples of $(Ga_{1-x}Zn_x)(N_{1-x}O_x)$ NCs. The first was made at 800 °C (x = 0.44) and consisted of particles with a homogeneous elemental distribution.[17] The second sample was made at 650 °C with a high x value (0.9), which are conditions that lead to a heterogeneous core−shell-like composition of individual particles and little particle-to-particle variation.[17] The final sample was made at 650 °C with x = 0.49, which are conditions that lead to the highest degree of compositional heterogeneity with heterogeneous compositions within particles and compositional variation from particle to particle.[17] The synthesis of these samples is described in the Experimental Section. As described in the Results and Discussion section, VEELS experiments reveal a range of behaviors, from single-band-gap electronic spectra with little spatial variation for the first sample, to two-band-gap spectra with little variation for the second sample, and, finally, to significant spatial variation in the VEELS spectra encompassing both types of electronic spectra. We discuss what these results teach us about the electronic heterogeneities in $(Ga_{1-x}Zn_x)(N_{1-x}O_x)$ NC materials and their intrinsic optical properties.

EXPERIMENTAL SECTION

Benzyl ether (98%), hexane (99%), toluene (99.5%), zinc acetylacetonate hydrate (Zn(acac)2, 99.995%), zinc chloride ($ZnCl_2$, ≥98%), gallium acetylacetonate (Ga(acac)3, 99.99%), 3-mercaptopropionic acid (3-MPA, ≥99.0%), 1,2-hexadecanediol (90%), oleic acid (≥99.0%), oleylamine (70%), and tetramethylammonium hydroxide pentahydrate (TMAH, ≥97%) were purchased from Sigma-Aldrich. 1,2-Ethanediol (99.8%) was purchased from Macron Fine Chemicals. Ethanol (95%) was purchased from Decon Laboratories. Methanol (99.9%), 2-propanol (99.9%), and sodium hydroxide (NaOH pellets, 99.3%) were purchased from Fisher. Ammonia (99.99%) was purchased from Airgas. All chemicals were used without further purification.

The synthesis of the x = 0.44 sample made at 800 °C was described previously,[17] and the same sample was used in this work. The x = 0.90 and 0.49 samples were synthesized at 650 °C from ZnO and $ZnGa_2O_4$ NC precursors as described below.

Synthesis of ZnO NCs. ZnO NCs were synthesized as described previously.[14,23] In summary, $ZnCl_2$ (40 mmol) was added to 1,2-ethanediol (200 mL) in a beaker and stirred until it dissolved. The mixture was heated to 150 °C. After reaching 150 °C, 5 M NaOH (16 mL) in water was added dropwise at a rate of ∼1 drop/s while maintaining a reaction temperature of 150 °C. When all of the 5 M NaOH was added, the solution was removed from heat and cooled to room temperature. The white powder product was first washed via sedimentation to remove NaCl in the reaction beaker by allowing the product to settle to the bottom of the beaker, then discarding the supernatant, and then filling the beaker with 18 MΩ water. Washing via sedimentation was repeated five times. After sedimentation, the white powder was collected via centrifugation (5000 rpm for 20 min) and washed an additional three times with water. The final white powder product was dried in the centrifuge tube using a vacuum desiccator.

Synthesis of $ZnGa_2O_4$ NCs. $ZnGa_2O_4$ NCs were synthesized by using a previously published method.[14] $Zn(acac)_2$ (1 mmol), $Ga(acac)_3$ (2 mmol), 1,2-hexadecanediol (5 mmol), oleic acid (6 mmol), and oleylamine (6 mmol) were combined in benzyl ether (10 mL) in a three-necked round-bottomed flask, stirred under $Ar_{(g)}$, and heated to 40 °C. Next, to remove O_2 and H_2O, the reaction was put under vacuum

https://doi.org/10.1021/acs.jpcc.3c00572
J. Phys. Chem. C 2023, 127, 7762−7771

and the temperature was increased to 100 °C. Once there was minimal bubbling of the reaction, the reaction was switched back to $Ar_{(g)}$ and the temperature was increased to 200 °C. After the reaction was held at 200 °C for 30 min, the reaction temperature was increased to 280 °C and held for 2 h. After 2 h, the reaction was removed from the heating mantle and cooled to room temperature. Then the NC product was collected using centrifugation and washed three times by dissolving in 5 mL of hexanes and precipitating with 45 mL of ethanol. After synthesis, the $ZnGa_2O_4$ NCs were capped using 3-MPA with a previously reported procedure.[14] 3-MPA (0.5 g) was dissolved in methanol (3 mL). TMAH was added until the pH reached 11 (1.61 g of TMAH). $ZnGa_2O_4$ NCs (60 mg) were dispersed in hexane (3 mL) and then precipitated with ethanol (15 mL). The basic 3-MPA solution was added to the $ZnGa_2O_4$ solution, and the mixture was shaken. When the mixture became optically clear, toluene (25 mL) was added to precipitate the ligand-exchanged $ZnGa_2O_4$, which was collected by centrifugation and dried under vacuum. The $ZnGa_2O_4$ NCs were dissolved in water (5 mL), washed with ethanol (15 mL) and toluene (25 mL) before being collected by centrifugation, and dried under vacuum.

Synthesis of $(Ga_{1-x}Zn_x)(N_{1-x}O_x)$ NCs. $(Ga_{1-x}Zn_x)(N_{1-x}O_x)$ NCs were synthesized as described previously.[14] Briefly, a total of ∼200 mg of $ZnGa_2O_4$ NC capped with 3-MPA and ZnO NC precursors was heated in a quartz tube furnace at 650 °C for 10 h under a flow of $NH_{3(g)}$ at ∼150 mL/min. The ratios of $ZnGa_2O_4$ NCs and ZnO NCs were varied to determine the final composition. The furnace was set to turn off after the desired reaction time, and the sample was left in the furnace overnight to cool under flowing $NH_{3(g)}$. In the morning, the $NH_{3(g)}$ was turned off and the furnace was purged with $Ar_{(g)}$ before opening. The alumina boats containing the product were removed from the furnace, and the product in the boats was carefully poured into a borosilicate vial.

Characterization of $(Ga_{1-x}Zn_x)(N_{1-x}O_x)$ NCs. The $(Ga_{1-x}Zn_x)(N_{1-x}O_x)$ NCs were characterized using inductively coupled plasma-optical emission spectroscopy (ICP-OES) to analyze the content of Zn and Ga. Diffuse reflectance spectroscopy was used to obtain a reflectance spectrum, which was converted into an absorbance spectrum using the Kubelka−Munk equation: $F(R_\infty) = (1 - R_\infty)^2/2R_\infty$, where $R_\infty = R_{sample}/R_{reference}$. Diffuse reflectance measurements were made on an Agilent Cary 60 UV−vis spectrophotometer with the Agilent Cary 60 Remote Diffuse Reflectance Accessory. A Spectralon puck was used as the reference.

Electron Energy Loss Spectroscopy. EELS data were collected on an FEI Titan Themis S/TEM equipped with a monochromator and a Gatan Quantum ERS electron spectrometer operated at 80 kV with energy dispersion per channel of 0.01 eV and a pixel dwell time of 0.002 s. The low accelerating voltage of 80 kV was selected to minimize Cherenkov radiation.[24−26] TEM samples were prepared either by picking up dry powder onto a holey carbon film supported by a 300-mesh copper TEM grid or by dropping the suspensions on an ultrathin carbon film TEM grid.

The EELS data were analyzed using HyperSpy, an open-source Python library.[27] A table of processing parameters is shown in Table S1. Our procedure for processing an EELS spectrum starts with aligning the zero-loss peak for all of the pixels in the spectrum image (Figures S1 and S2). The tail of the zero-loss peak from ∼1 to 3 eV is fitted with a power law and subtracted from the spectrum (Figure S3). Non-negative matrix factorization (NMF) is used to denoise the data. NMF decomposes the hyperspectral image into a user-defined number of spectral "factors/components" and associated "loadings". A typical data set is decomposed into between three and five different components until the last component appears to be noise. Then, the noise component is discarded and the spectrum is reconstructed with the remaining components and their associated loading. We compare the reconstructed spectra with the raw data to verify the integrity of the denoised spectra. (See Figure S4 as an example.) Following NMF, the data was imported into MATLAB. The baseline (2−2.3 eV) was fit linearly; this fit was subtracted from the entire spectra. For spectra with one onset, the "visible" portion of the spectrum (2.7−3.0 eV) was fit linearly. The intercept of the fit with the baseline was taken as the band gap. For spectra with two onsets, the "UV" portion of the spectrum (3.25−3.35 eV) was fit in addition to the visible section. The intercept of the 3.25−3.35 eV fit with the baseline was taken as the "UV" band gap, while the intercept of the 2.7−3.0 eV fit was taken as the "visible" band gap (Figure S5). This band gap fitting results in a band gap value for the spectra at each pixel. Color-coded band gap maps were plotted using the *pcolor* function in MATLAB. For clarity, sections of the band gap map outside of the edge of the particle were masked out (Figure S6). These data analysis steps are explained in detail in sections 1−7 (including Figures S7 and S8 and Table S2 in addition to those previously mentioned) of the Supporting Information.

RESULTS AND DISCUSSION

For each of the three samples described above, we used STEM-VEELS to collect high-resolution hyperspectral images, in which each pixel contains a spectrum covering the UV−vis region. EELS analyzes inelastic scattering events that occur when the electron beam passes through the sample, and VEELS uses a monochromated electron beam to achieve sufficient energy resolution to analyze relatively low-energy transitions such as plasmons,[28−31] band gap transitions,[32−38] and even vibrational transitions.[39−41] Due to the technical requirements, VEELS has not yet been widely adopted for studying the electronic structure of semiconductor NCs.[34,42−44] Consequently, the effects of sample thickness, Coulomb delocalization, and Cherenkov radiation are not well understood, and the ultimate spatial resolution of the technique for this class of materials is still under debate.[45,46] We systematically investigated the consequences of these factors and determined the spatial resolution of our measurements, defined as the full-width at half-maximum electron delocalization diameter, to be 8 nm (Figure S7). The energy resolution was 80 meV, and the energy precision, based on the standard deviation of band gap measurements, was 10 meV (Figures S1 and S2). The spatial resolution is limited by Coulomb delocalization caused by the long-range Coulomb interaction between the electron beam and the valence electrons of atoms, which makes the spatial resolution of VEELS significantly worse than those of other STEM experiments.[46] The practical implication of this delocalization for the $(Ga_{1-x}Zn_x)(N_{1-x}O_x)$ NCs studied here is that VEELS robustly reports single-particle absorption spectra while the spatial variation in absorption within each particle stretches the limits of the spatial resolution of this experiment.

https://doi.org/10.1021/acs.jpcc.3c00572
J. Phys. Chem. C 2023, 127, 7762−7771

We start our discussion with a sample of $(Ga_{1-x}Zn_x)$-$(N_{1-x}O_x)$ NCs synthesized at 800 °C. Our group has previously described the synthesis, optical, STEM-EDS, and powder X-ray diffraction characterization of such NCs,[17] and here we summarize the most salient points. Most importantly for our discussion, as shown in Figure 1, at this synthesis temperature, Zn and Ga are homogeneously distributed throughout the particles over a range of compositions (x = 0.11−0.44). O and N positions correlate with the Zn and Ga positions, respectively, and these particles are single-crystalline.[17] Additionally, the local particle composition obtained from the quantification of STEM-EDS data matched the ensemble compositions measured by ICP-OES, meaning that the ensemble composition accurately describes the local composition of individual particles.[17] For the discussion here, we chose the particles with the composition $(Ga_{0.56}Zn_{0.44})$-$(N_{0.56}O_{0.44})$, i.e., x = 0.44, and average diameters of 34.7 ± 12.0 nm, which were previously characterized in detail.[17]

In Figure 2, we show VEELS spectra from four points on the annular dark field (ADF)-STEM image of this sample (shown in the inset). For each point, the inner circle marks the position from where the spectrum is collected, and the larger transparent circle indicates the Coulomb delocalization diameter that determines the spatial resolution of the VEELS signal. The four points in Figure 2 are sufficiently spaced to minimize the influence of Coulomb delocalization. The VEELS spectra are almost identical to each other, suggesting similarities in the electronic structure across the sample that one would expect to see with homogeneous composition. They feature a sloping onset that begins at ∼2.5 eV, corresponding to the visible band gap. Figure 2 also shows the absorption spectrum of the ensemble sample measured by diffuse reflectance spectroscopy, which is qualitatively similar to the VEELS spectra and also shows a visible band gap of ∼2.5 eV.

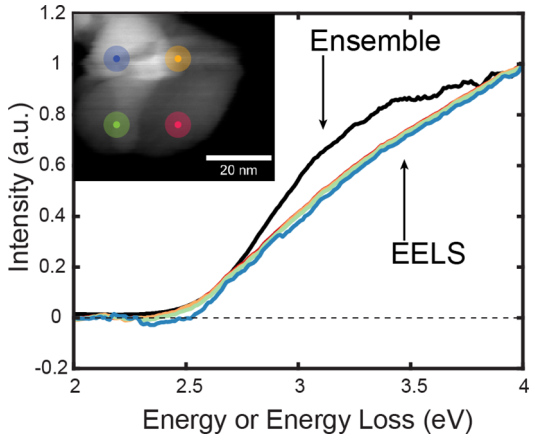

Figure 2. VEELS spectra collected at four points marked on the ADF-STEM image in the inset and the ensemble diffuse reflectance spectrum (black). Spectra are normalized at 4 eV. The larger circles show the Coulomb delocalization limiting the spatial resolution of the VEELS measurements.

To investigate how the VEELS spectra and band gaps vary across mapping regions, we simultaneously examine thousands of spectra contained in three EELS maps. As suggested by Figure 2, the VEELS spectra are qualitatively similar to each other with a single visible band gap that coincides with the measured band gap from the ensemble absorption spectrum, which is also shown with the VEELS spectra of Figure 3. In Figure 3a,c, the thousands of VEELS spectra line up in terms of shape and position. The region in Figure 3b shows the largest degree of variation among the spectra, but they still show a single visible band gap at around 2.5 eV. To compare these large numbers of spectra quantitatively and spatially, we devised a MATLAB routine to linearly fit the baseline and absorption onsets for each spectrum and defined the band gap as the intercept of the onset fits with the baseline (Figure S5). With values of the band gap at each pixel, we produced band gap maps, shown in Figure 3a−c (right). For all three regions, there is minimal band gap variation, with average values of 2.52 ± 0.01, 2.51 ± 0.02, and 2.49 ± 0.01 (see inset histograms or Table S1), where the error is the standard deviation. In Figure 3b, there is a region with somewhat lower band gaps, closer to 2.45 eV, on the lower left, which accounts for a somewhat wider standard deviation. Overall, these results demonstrate that for the compositionally homogeneous $(Ga_{1-x}Zn_x)$-$(N_{1-x}O_x)$ NC sample, the VEELS spectra and therefore electronic structure have only minor spatial variations in the spectra and band gap energies.

Now we turn our attention to a more interesting $(Ga_{1-x}Zn_x)(N_{1-x}O_x)$ sample, synthesized at 650 °C with an x value of 0.90, as determined by elemental analysis of the ensemble sample. Figure 4a,b shows typical high-resolution bright field STEM (BF-STEM) and ADF-STEM images of this sample. As we described previously, at this relatively low synthesis temperature, Ga and N do not fully diffuse into the ZnO precursor particles, resulting in a heterogeneous elemental distribution.[17] At high x values, ∼0.9, the samples consist of core−shell-like particles with Zn-rich cores and Ga-rich shells. The quantification of STEM-EDS images showed that at the high x values the composition of individual NCs matches the ensemble composition.[17] In other words, the composition is heterogeneous within each particle but similar from particle to particle. These samples have qualitatively different ensemble absorption spectra than those in Figures 2 and 3. As shown in Figure 4c, we observe two absorption onsets indicative of two band gaps, one in the visible region and one in the UV region, similar to what was reported previously.[15,47] This absorption spectrum brings up a key question about this set of $(Ga_{1-x}Zn_x)(N_{1-x}O_x)$ NCs: is the ensemble optical spectrum with two onset energies a sum of two types of spectra originating from different particles or different regions within each particle, or does the ensemble spectrum reflect the absorption of individual particles?

We address this question using the VEELS methods described above. In Figure 4c, we show four EELS spectra from four locations across the sample. As before, these points are sufficiently spaced to reduce the influence of Coulomb delocalization, and the delocalization length is indicated by the transparent circles surrounding each point. The VEELS spectra at all four points overlap very well. Moreover, they are qualitatively similar to the ensemble absorption spectrum and show both visible and UV onset. The persistence of the dual-onset spectral shape across the sample is remarkable and warrants further investigation.

As we did for the previous sample, we analyzed hyperspectral images collected over multiple particles, as shown in Figure 5a,b. In both regions, the spectra overlap considerably, indicating that the two absorption onsets are observed across the entire mapping regions. Note that due to the Coulomb delocalization diameter of 8 nm we cannot confidently isolate the VEELS spectra of the thin shell regions from the core

https://doi.org/10.1021/acs.jpcc.3c00572
J. Phys. Chem. C 2023, 127, 7762−7771

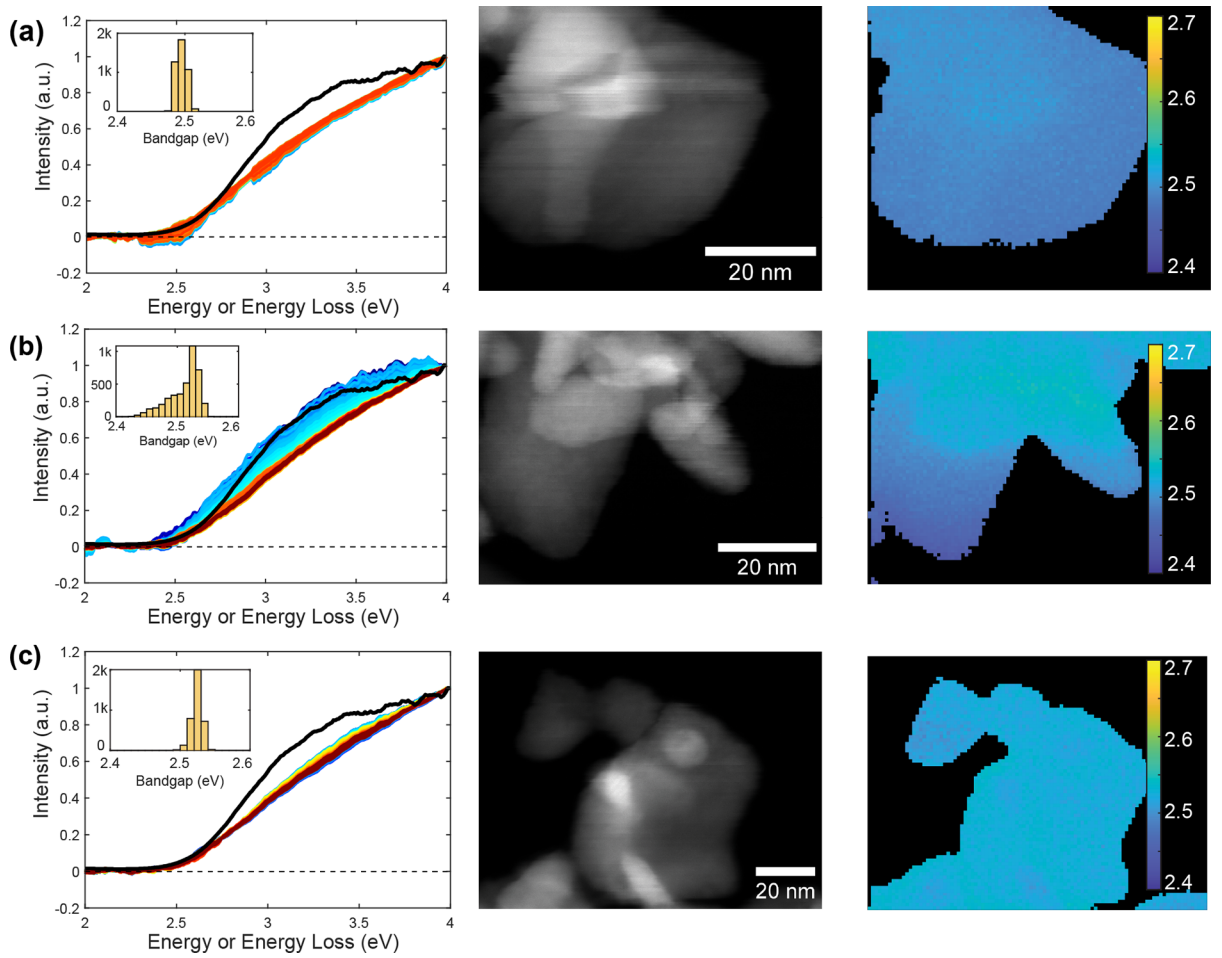

Figure 3. Data from three regions of the $(Ga_{1-x}Zn_x)(N_{1-x}O_x)$ NC (x = 0.44) sample synthesized at 800 °C. (Left) Ensemble diffuse reflectance spectra in black compared to all VEELS spectra (4252 spectra in (a), 4010 spectra in (b), and 3675 spectra in (c)) collected from the regions shown in the ADF-STEM images in the middle column. Spectra are normalized at 4 eV. Insets show histograms of the visible band gaps for the maps. The histogram bin width was 0.01 eV. (Right) Maps of visible band gap energies, as determined by fitting the absorption onset in the VEELS spectra. Color bars are in units of eV. For clarity, pixels outside of the particle are masked, as described in Figure S6.

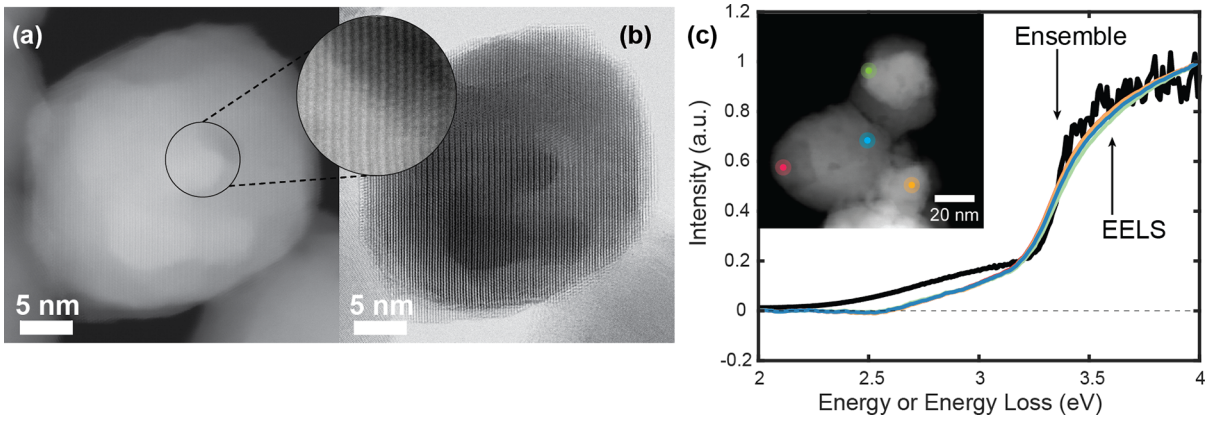

Figure 4. (a) ADF-STEM and (b) BF-STEM images of the $(Ga_{0.10}Zn_{0.90})(N_{0.10}O_{0.90})$ sample synthesized at 650 °C. The inset shows the lattice fringes in the ADF-STEM image. (c) Ensemble diffuse reflectance spectrum (black) compared to VEELS spectra collected at four points shown in the inset. Spectra are normalized at 4 eV.

regions. It is possible that there are no spatial differences in the VEELS spectra across the particle, and it is also possible that differences that exist are not apparent because of the spatial convolution of the VEELS signals due to Coulomb delocalization and the presence of the shell above the core. We can, however, see whether different particles have significantly different VEELS spectra. They do not. As we did for the previous sample, we used a MATLAB procedure to extract the absorption onsets of these spectra. To extract both apparent band gaps, we fit the visible (2.7−3.0 eV) and UV

https://doi.org/10.1021/acs.jpcc.3c00572
J. Phys. Chem. C 2023, 127, 7762−7771

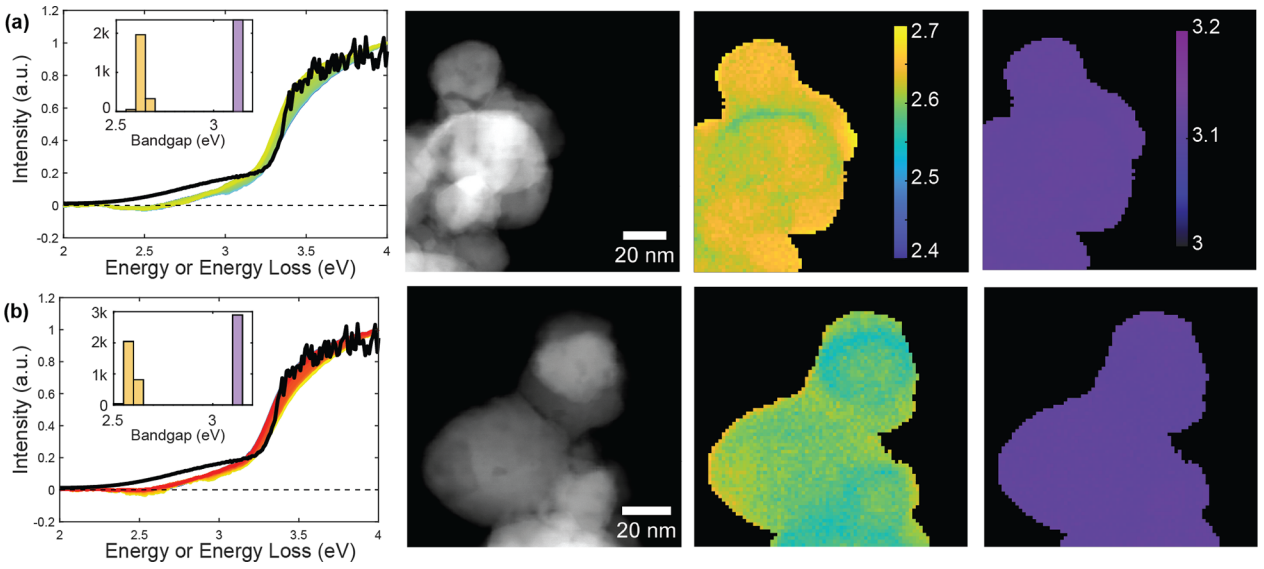

Figure 5. (a) (Left) Ensemble diffuse reflectance trace in black compared to 2341 VEELS spectra collected within the NCs. Spectra are normalized at 4 eV. (Inset) Histogram of the extracted visible and UV band gaps. The histogram bin width was 0.05 eV. (Middle) ADF-STEM image of the examined region. (Right) Visible and UV band gap maps determined as described in the text. Color bars are in units of eV. For clarity, pixels outside of the particle are masked, as described in Figure S6. (b) Similar to (a) but with data from another region of the sample and 2893 VEELS spectra.

(3.25−3.35 eV) parts of the VEELS spectra and produced band gap maps (right panels of Figure 5a,b) and histograms (insets in the left panels of Figure 5a,b). The region in Figure 5a shows a visible band gap of 2.64 ± 0.02 eV and Figure 5b has the visible band gap of 2.59 ± 0.02 eV, while the UV band gaps are 3.12 ± 0.00 and 3.11 ± 0.00 eV, respectively.

Given the strong dependence of the ensemble absorption spectra of $(Ga_{1-x}Zn_x)(N_{1-x}O_x)$ on the ensemble composition,[15] the compositional heterogeneity within each particle,[17] and the complexity of the absorption spectrum with two clear onsets,[15,47] the similarities in the VEELS spectra across multiparticle regions and their similarities to the ensemble absorption spectrum are remarkable. These similarities indicate that the electronic structure reflected by the ensemble spectra persists over the individual particles. In other words, it is not the case that the absorption spectra of the ensemble are simply the sum of the absorption spectra of particles, some with visible and some with UV band gaps. Rather, each particle has both the visible and the UV band gap. This conclusion is consistent with our prior work on the time-resolved spectroscopy of $(Ga_{0.27}Zn_{0.73})(N_{0.27}O_{0.73})$ NCs, synthesized at 650 °C, which had distinct visible and UV bleach transitions in the transient absorption spectra.[47] The two transitions had overlapping decay kinetics, suggesting that they originated from two band gaps on each particle, each featuring a different valence band and sharing a conduction band. The spatial persistence of the two-onset VEELS spectra supports the conclusion that each particle has two band gaps. Furthermore, the narrow range of band gap energies that we observe and the lack of spatial variation in absorption onset (within our experimental resolution) are both inconsistent with the short-range order model of the visible absorption that was proposed for $(Ga_{1-x}Zn_x)(N_{1-x}O_x)$ nanowires.[6] In this model, the visible absorption is proposed to originate from interfacial transitions between small regions of quantum-confined GaN and ZnO.[6] One would expect these GaN/ZnO domains to vary in size; consequently, the electronic transition energies would vary with domain size, resulting in a broad range and spatial variation of the band gap energies. Instead, we observe a narrow range of band gap energies with minimal spatial variation (Figures 3 and 5).

As a point of comparison, VEELS experiments have been carried out on bulk $(Ga_{0.15}Zn_{0.85})(N_{0.15}O_{0.85})$ thin films synthesized by RF magnetron sputtering with a homogeneous composition.[13] Although the composition is similar to that of the $(Ga_{0.10}Zn_{0.90})(N_{0.10}O_{0.90})$ NCs described here, the VEELS spectra for those samples had a single onset at ∼2.5 eV, rather than two onsets, and showed a much wider variation in onsets (±0.25 eV). The significant qualitative difference in the VEELS spectra of the two types of $(Ga_{1-x}Zn_x)(N_{1-x}O_x)$ materials may be due to the core−shell-like nature of the NCs we describe here versus the homogeneous composition of the bulk $(Ga_{0.15}Zn_{0.85})(N_{0.15}O_{0.85})$. This contrast reveals that there are significant differences in electronic structure between $(Ga_{1-x}Zn_x)(N_{1-x}O_x)$ made by different methods and highlights the unique properties of $(Ga_{1-x}Zn_x)(N_{1-x}O_x)$ NCs.

For the last part of our discussion, we focus on a sample of $(Ga_{1-x}Zn_x)(N_{1-x}O_x)$ NCs synthesized at 650 °C with the ensemble composition of $x = 0.49$ as determined by ICP-OES. We have previously shown that for the samples of $(Ga_{1-x}Zn_x)$-$(N_{1-x}O_x)$ NCs synthesized at 650 °C with intermediate compositions ($x \approx 0.5$), the composition of individual NCs can vary dramatically from the ensemble composition.[17] This is due to the presence of at least two types of particles: the core−shell-like ones, such as the $x = 0.9$ sample above with diameters of ∼20 nm, and smaller (∼5 nm) ones with a homogeneous composition.[17] In other words, in these materials the elemental composition is not only heterogeneous within individual NCs (intraparticle heterogeneity) but heterogeneous across the ensemble (interparticle heterogeneity). Core-loss compositional EELS analysis on this sample, shown in Figure S9, illustrates the core−shell-like heterogeneity.

Figure 6 shows the VEELS spectra of this sample collected across a region shown in the inset of the ADF-STEM image

https://doi.org/10.1021/acs.jpcc.3c00572
J. Phys. Chem. C 2023, 127, 7762−7771

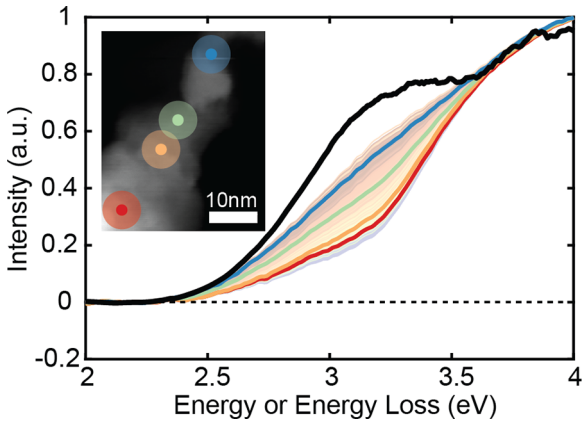

Figure 6. $(Ga_{1-x}Zn_x)(N_{1-x}O_x)$ NC sample with $x = 0.49$ synthesized at 650 °C: VEELS spectra from the pixels in the mapping region, with pixels outside the particles masked out, (transparent colors), four highlighted points labeled in the inset ADF-STEM image, and the ensemble optical spectrum (black). Spectra are normalized at 4 eV. While the ensemble spectrum has only one onset, there is a gradient from one to two onsets in the VEELS spectra.

and the ensemble absorption spectrum (black). Unlike the two samples discussed above, here we see significant spatial variation in the VEELS spectra. The four highlighted VEELS spectra from four distinct locations in the imaged region range from a single-onset shape with an onset of around 2.4 eV to a two-onset shape with a visible and a UV band gap (Figure 6). The 3994 VEELS spectra shown in Figure 6 show a gradient of spectral shape between these two extremes and suggest a significant qualitative variation in the electronic structure across the sample. Within the Coulomb-delocalization-determined spatial resolution of ∼8 nm, the spectral gradient across the sample is what we expect to see when the individual particles in the image have different VEELS spectra. The data reveal that, for this sample with intraparticle and interparticle compositional heterogeneity, the ensemble absorption spectrum is not a reflection of the spectra of individual particles but rather a sum of contributions from particles with different electronic structure. Such electronic heterogeneity has not been reported in bulk $(Ga_{1-x}Zn_x)(N_{1-x}O_x)$ and is likely a direct consequence of the mechanism of the solid-state reaction that produces $(Ga_{1-x}Zn_x)(N_{1-x}O_x)$ NCs.

As shown in Figure 7a, there is a correlation between the position and the VEELS spectral shape. On the particle in the upper right of the ADF-STEM image (Figure 7b), the VEELS spectra in Figure 7a resemble the single visible band gap shape of the sample made at 800 °C (Figures 2 and 3). The particle area on the lower left has the two band gap shape more akin to that of the $x = 0.9$ sample made at 650 °C (Figures 4 and 5). In all of the spectra, the intercept of the visible onset, calculated by linear fitting of the 2.6−3.0 eV region, shows little variation (2.49 ± 0.01 eV). What varies with position is the fraction of the UV band gap component of the VEELS spectrum. To quantitatively describe the spatial variation in the VEELS spectral shape, we analyze the data as follows: For the single-onset spectral shape, the linear fit from the visible portion of the spectrum fits the entire spectrum from 2.5 to 4.0 eV reasonably well and the area under the linear fit roughly matches the area under the VEELS spectrum. For the two-onset spectral shape, the linear fit fits the spectrum well from 2.5 to 3 eV but diverges in the 3 to 4 eV region because of the second absorption onset in the UV. For each of the VEELS spectra, we define a parameter S, which is a ratio of the area under the linear fit of 2.5−4.0 eV and the area under the total VEELS spectrum. In other words, S is approximately a measure of what fraction of the total VEELS spectrum is due to the absorption from the single onset spectral shape (Figure S10). To see how S is calculated, see section 9 of the Supporting Information. Figure 7c shows a map of the S values. Pixels with $S \approx 1$ correspond to single-onset spectral shapes, while lower S values denote the presence of the UV onset, with S values decreasing with an increasing proportion of the UV-onset component. The map in Figure 7c quantitatively shows that the $(Ga_{1-x}Zn_x)(N_{1-x}O_x)$ particle in the upper part of the image has a distinct electronic spectrum from that of the particle in the lower half. Based on our prior STEM-EDS work,[17] we suspect that the upper particle has a homogeneous composition, hence the spectrum resembles that of homogeneous particles, while the lower one has the core−shell-like elemental distribution such as for the particles in Figures 4 and 5, hence the two band gaps. The electronic structure heterogeneity in this sample complicates applications such as solar water splitting because it is quite possible that the two types of particles would have different photochemical activities

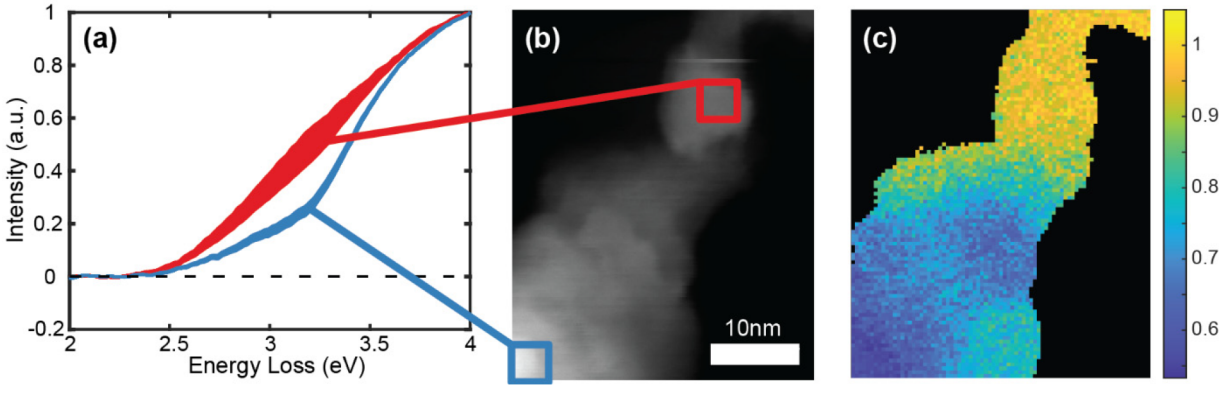

Figure 7. $(Ga_{1-x}Zn_x)(N_{1-x}O_x)$ NC sample with $x = 0.49$ synthesized at 650 °C: (a) VEELS spectra taken from the top (red) and bottom (blue) regions shown in the ADF-STEM image in (b). Spectra are normalized at 4 eV. (c) Map of the spectral shape parameter S. Lower values or more blue pixels correspond to a two-onset spectral shape, while higher values or more yellow pixels correspond to a single-onset spectral shape. For clarity, pixels outside of the particle are masked, as described in Figure S6.

https://doi.org/10.1021/acs.jpcc.3c00572
J. Phys. Chem. C 2023, 127, 7762−7771

that would be averaged in ensemble product formation measurements.

CONCLUSIONS

We have used VEELS to examine the local electronic structure of three different samples of $(Ga_{1-x}Zn_x)(N_{1-x}O_x)$ NCs, which show increasing degrees of compositional heterogeneity: one where the composition is homogeneous throughout each particle and from particle to particle, one with a heterogeneous core−shell-like composition within each particle but little particle-to-particle variation, and one where both the intraparticle composition and interparticle composition are heterogeneous. In the first case, we observe a high degree of similarity in VEELS spectra across analyzed regions and qualitative similarity between the VEELS spectra and the ensemble absorption spectrum. More interestingly, in the second case, we observe a similar scenario, with little spatial variation in VEELS spectra and high degree of similarity to the ensemble absorption spectrum. This indicates that the ensemble absorption spectrum reflecting two distinct band gaps is representative of the spectra of individual particles rather than a sum of spectra of particles with distinct electronic structure. Moreover, the VEELS spectra provide experimental evidence of the dual-band-gap electronic structure previously proposed for $(Ga_{1-x}Zn_x)(N_{1-x}O_x)$ NCs.[15,47,48] Finally, in the third case, we observe spatial variation in the VEELS spectra, with spectra ranging from containing a single visible band gap to containing both the visible and the UV band gaps. In this case, the VEELS data indicates that the ensemble absorption spectrum does not reflect the spectra of individual particles but rather is a sum of spectra from particles with varying electronic structure. Remarkably, the visible absorption persists throughout all of the samples and regions examined in this work, with the most prominent variation being that of the relative strengths of the absorption in the visible and UV regions. Our work illustrates the importance of nanoscale compositional heterogeneity in determining the optical properties of these compositionally complex nanomaterials. More generally, we illustrate that VEELS is a powerful tool for characterizing ternary or quaternary nanocrystal alloys, where particle-to-particle heterogeneity may influence the optical properties of the ensemble but is obscured in ensemble optical measurements.

ASSOCIATED CONTENT

Supporting Information

The Supporting Information is available free of charge at https://pubs.acs.org/doi/10.1021/acs.jpcc.3c00572.

Table of data processing parameters and results, description of zero-loss peak alignment, zero-loss peak background subtraction, denoising by non-negative matrix factorization, extraction of band gaps from VEELS spectra, masking process, theoretical calculation and experimental measurement of spatial resolution, measurement of beam broadening due to sample thickness, core-loss EELS maps and spectra from the $x = 0.49$ $(Ga_{1-x}Zn_x)(N_{1-x}O_x)$ NC sample, and calculation and graphical representation of the spectral shape parameter, S (PDF)

AUTHOR INFORMATION

Corresponding Author

Gordana Dukovic − *Materials Science and Engineering, Department of Chemistry, and Renewable and Sustainable Energy Institute, University of Colorado, Boulder, Colorado 80309-0215, United States;* orcid.org/0000-0001-5102-0958; Email: gordana.dukovic@colorado.edu

Authors

Benjamin F. Hammel − *Materials Science and Engineering, University of Colorado, Boulder, Colorado 80309-0215, United States*

Leah M. G. Hall − *Department of Chemistry, University of Colorado, Boulder, Colorado 80309-0215, United States*

Lauren M. Pellows − *Department of Chemistry, University of Colorado, Boulder, Colorado 80309-0215, United States;* orcid.org/0000-0002-1088-1898

Orion M. Pearce − *Department of Chemistry, University of Colorado, Boulder, Colorado 80309-0215, United States;* Present Address: Department of Chemistry and Physics, North Central College, Naperville, Illinois 60540-4607, United States

Pornthip Tongying − *Department of Chemistry, University of Colorado, Boulder, Colorado 80309-0215, United States;* Present Address: Department of Chemistry, Faculty of Science, Silpakorn University, Nakhon Pathom, 73000 Thailand.

Sadegh Yazdi − *Materials Science and Engineering and Renewable and Sustainable Energy Institute, University of Colorado, Boulder, Colorado 80309-0215, United States;* orcid.org/0000-0002-3470-9398

Complete contact information is available at: https://pubs.acs.org/10.1021/acs.jpcc.3c00572

Author Contributions

‖B.F.H. and L.M.G.H. contributed equally.

Notes

The authors declare no competing financial interest.

ACKNOWLEDGMENTS

This work was supported by the National Science Foundation under STROBE grant no. DMR 1548924. Support is acknowledged from the Facility for Electron Microscopy of Materials at the University of Colorado at Boulder (CU FEMM, RRID: SCR_019306).

REFERENCES

(1) Maeda, K.; Teramura, K.; Lu, D.; Takata, T.; Saito, N.; Inoue, Y.; Domen, K. Photocatalyst Releasing Hydrogen from Water. *Nature* **2006**, *440*, 295−295.

(2) Maeda, K.; Takata, T.; Hara, M.; Saito, N.; Inoue, Y.; Kobayashi, H.; Domen, K. GaN:ZnO Solid Solution as a Photocatalyst for Visible-Light-Driven Overall Water Splitting. *J. Am. Chem. Soc.* **2005**, *127*, 8286−8287.

(3) Liu, J.; Fernández-Serra, M. V.; Allen, P. B. Special Quasiordered Structures: Role of Short-Range Order in the Semiconductor Alloy $(GaN)_{1-x}(ZnO)_x$. *Phys. Rev. B* **2016**, *93*, No. 054207.

(4) Kraut, M.; Sirotti, E.; Pantle, F.; Jiang, C.-M.; Groetzner, G.; Koch, M.; Wagner, I.; Sharp, I. D.; Stutzmann, M. Control of Band Gap and Band Edge Positions in Gallium-Zinc Oxynitride Grown by Molecular Beam Epitaxy. *J. Phys. Chem. C* **2020**, *124*, 7668−7676.

(5) Yang, C.; Hirose, Y.; Wakasugi, T.; Kashiwa, N.; Kawai, H.; Yamashita, K.; Hasegawa, T. Epitaxy of $(GaN)_{1-x}(ZnO)_x$ Solid-Solution Thin Films with Widely Tunable Chemical Composition and

Strong Visible Absorption. *Phys. Rev. Applied* **2018**, *10*, DOI: 10.1103/PhysRevApplied.10.044001.
(6) Zhang, K.; Chen, T.; Abbas, Y.; Jan, S. U.; Zhou, Z.; Chu, S.; Xie, G.; Ullah, S.; Akram, M. Z.; Zhang, J. Atomic Arrangement Matters: Band-Gap Variation in Composition-Tunable $(Ga_{1-x}Zn_x)(N_{1-x}O_x)$ Nanowires. *Matter* **2021**, *4*, 1054.
(7) Li, Y.; Zhu, L.; Yang, Y.; Song, H.; Lou, Z.; Guo, Y.; Ye, Z. A Full Compositional Range for a $(Ga_{1-x}Zn_x)(N_{1-x}O_x)$ Nanostructure: High Efficiency for Overall Water Splitting and Optical Properties. *Small* **2015**, *11*, 871−876.
(8) Nakada, A.; Kuriki, R.; Sekizawa, K.; Nishioka, S.; Vequizo, J. J. M.; Uchiyama, T.; Kawakami, N.; Lu, D.; Yamakata, A.; Uchimoto, Y.; et al. Effects of Interfacial Electron Transfer in Metal Complex-Semiconductor Hybrid Photocatalysts on Z-Scheme CO_2 Reduction under Visible Light. *ACS Catal.* **2018**, *8*, 9744−9754.
(9) Kosem, N.; Honda, Y.; Watanabe, M.; Takagaki, A.; Tehrani, Z. P.; Haydous, F.; Lippert, T.; Ishihara, T. Photobiocatalytic H_2 Evolution of GaN:ZnO and [FeFe]-Hydrogenase Recombinant Escherichia Coli. *Catal. Sci. Technol.* **2020**, *10*, 4042−4052.
(10) Maeda, K.; Domen, K. Solid Solution of GaN and ZnO as a Stable Photocatalyst for Overall Water Splitting under Visible Light. *Chem. Mater.* **2010**, *22*, 612−623.
(11) Maiti, D.; Cairns, J.; Kuhn, J. N.; Bhethanabotla, V. R. Interface Engineering of Metal Oxynitride Lateral Heterojunctions for Photocatalytic and Optoelectronic Applications. *J. Phys. Chem. C* **2018**, *122*, 22504−22511.
(12) Maiti, D.; Meier, A. J.; Cairns, J.; Ramani, S.; Martinet, K.; Kuhn, J. N.; Bhethanabotla, V. R. Intrinsically Strained Noble Metal-Free Oxynitrides for Solar Photoreduction of CO_2. *Dalton T* **2019**, *48*, 12738−12748.
(13) Olsen, V. S.; Baldissera, G.; Zimmermann, C.; Granerød, C. S.; Bazioti, C.; Galeckas, A.; Svensson, B. G.; Kuznetsov, A. Yu.; Persson, C.; Prytz, Ø.; et al. Evidence of Defect Band Mechanism Responsible for Band Gap Evolution in $(ZnO)_{1-x}(GaN)_x$ Alloys. *Phys. Rev. B* **2019**, *100*, No. 165201.
(14) Lee, K.; Tienes, B. M.; Wilker, M. B.; Schnitzenbaumer, K. J.; Dukovic, G. $(Ga_{1-x}Zn_x)(N_{1-x}O_x)$ Nanocrystals: Visible Absorbers with Tunable Composition and Absorption Spectra. *Nano Lett.* **2012**, *12*, 3268−3272.
(15) Lee, K.; Lu, Y.-G.; Chuang, C.-H.; Ciston, J.; Dukovic, G. Synthesis and Characterization of $(Ga_{1-x}Zn_x(N_{1-x}O_x)$ Nanocrystals with a Wide Range of Compositions. *J. Mater. Chem. A* **2016**, *4*, 2927−2935.
(16) Chen, H.; Wen, W.; Wang, Q.; Hanson, J. C.; Muckerman, J. T.; Fujita, E.; Frenkel, A. I.; Rodriguez, J. A. Preparation of $(Ga_{1-x}Zn_x)(N_{1-x}O_x)$ Photocatalysts from the Reaction of NH_3 with Ga_2O_3/ZnO and $ZnGa_2O_4$: In Situ Time-Resolved XRD and XAFS Studies. *J. Phys. Chem. C* **2009**, *113*, 3650−3659.
(17) Tongying, P.; Lu, Y.-G.; Hall, L. M. G.; Lee, K.; Sulima, M.; Ciston, J.; Dukovic, G. Control of Elemental Distribution in the Nanoscale Solid-State Reaction That Produces $(Ga_{1-x}Zn_x)(N_{1-x}O_x)$ Nanocrystals. *ACS Nano* **2017**, *11*, 8401−8412.
(18) Yarema, O.; Yarema, M.; Wood, V. Tuning the Composition of Multicomponent Semiconductor Nanocrystals: The Case of I−III−VI Materials. *Chem. Mater.* **2018**, *30*, 1446−1461.
(19) Wang, Q.; Domen, K. Particulate Photocatalysts for Light-Driven Water Splitting: Mechanisms, Challenges, and Design Strategies. *Chem. Rev.* **2020**, *120*, 919−985.
(20) Ismail, A. A.; Bahnemann, D. W. Photochemical Splitting of Water for Hydrogen Production by Photocatalysis: A Review. *Sol Energ Mat Sol C* **2014**, *128*, 85−101.
(21) Cook, T. R.; Dogutan, D. K.; Reece, S. Y.; Surendranath, Y.; Teets, T. S.; Nocera, D. G. Solar Energy Supply and Storage for the Legacy and Nonlegacy Worlds. *Chem. Rev.* **2010**, *110*, 6474−6502.
(22) Walter, M. G.; Warren, E. L.; McKone, J. R.; Boettcher, S. W.; Mi, Q.; Santori, E. A.; Lewis, N. S. Solar Water Splitting Cells. *Chem. Rev.* **2010**, *110*, 6446−6473.
(23) Becheri, A.; Dürr, M.; Nostro, P. L.; Baglioni, P. Synthesis and Characterization of Zinc Oxide Nanoparticles: Application to Textiles as UV-Absorbers. *J. Nanopart. Res.* **2008**, *10*, 679−689.
(24) Kadkhodazadeh, S.; Ashwin, M. J.; Jones, T. S.; McComb, D. W. Towards Measuring Bandgap Inhomogeneities in InAs/GaAs Quantum Dots. *J. Phys. Conf Ser.* **2008**, *126*, No. 012049.
(25) Zhan, W.; Venkatachalapathy, V.; Aarholt, T.; Kuznetsov, A. Y.; Prytz, Ø. Band Gap Maps beyond the Delocalization Limit: Correlation between Optical Band Gaps and Plasmon Energies at the Nanoscale. *Sci. Rep* **2018**, *8*, 848.
(26) Zhan, W.; Kosinskiy, A. Y.; Vines, L.; Johansen, K. M.; Carvalho, P. A.; Prytz, Ø. $ZnCr_2O_4$ Inclusions in ZnO Matrix Investigated by Probe-Corrected STEM-EELS. *Materials* **2019**, *12*, 888.
(27) Peña, F. de la; Prestat, E.; Fauske, V. T.; Burdet, P.; Lähnemann, J.; Jokubauskas, P.; Furnival, T.; Nord, M.; Ostasevicius, T.; MacArthur, K. E. et al. *Hyperspy/Hyperspy*, Release v1.7.0; Zenodo, 2022.
(28) Nicoletti, O.; Peña, F. de la; Leary, R. K.; Holland, D. J.; Ducati, C.; Midgley, P. A. Three-Dimensional Imaging of Localized Surface Plasmon Resonances of Metal Nanoparticles. *Nature* **2013**, *502*, 80−84.
(29) Yazdi, S.; Daniel, J. R.; Large, N.; Schatz, G. C.; Boudreau, D.; Ringe, E. Reversible Shape and Plasmon Tuning in Hollow AgAu Nanorods. *Nano Lett.* **2016**, *16*, 6939−6945.
(30) Scholl, J. A.; Koh, A. L.; Dionne, J. A. Quantum Plasmon Resonances of Individual Metallic Nanoparticles. *Nature* **2012**, *483*, 421−427.
(31) Moradifar, P.; Nixon, A. G.; Sharifi, T.; Driel, T. B.; Ajayan, P.; Masiello, D. J.; Alem, N. Nanoscale Mapping and Defect-Assisted Manipulation of Surface Plasmon Resonances in 2D Bi2Te3/Sb2Te3 In-Plane Heterostructures. *Adv. Opt Mater.* **2022**, *10*, 2101968.
(32) Granerød, C. S.; Zhan, W.; Prytz, Ø. Automated Approaches for Band Gap Mapping in STEM-EELS. *Ultramicroscopy* **2018**, *184*, 39−45.
(33) Tizei, L. H. G.; Lin, Y.-C.; Mukai, M.; Sawada, H.; Lu, A.-Y.; Li, L.-J.; Kimoto, K.; Suenaga, K. Exciton Mapping at Subwavelength Scales in Two-Dimensional Materials. *Phys. Rev. Lett.* **2015**, *114*, No. 107601.
(34) Jung, H. J.; Dasgupta, N. P.; Van Stockum, P. B.; Koh, A. L.; Sinclair, R.; Prinz, F. B. Spatial Variation of Available Electronic Excitations within Individual Quantum Dots. *Nano Lett.* **2013**, *13*, 716−721.
(35) Bosman, M.; Tang, L. J.; Ye, J. D.; Tan, S. T.; Zhang, Y.; Keast, V. J. Nanoscale Band Gap Spectroscopy on ZnO and GaN-Based Compounds with a Monochromated Electron Microscope. *Appl. Phys. Lett.* **2009**, *95*, 101110.
(36) Martí-Sánchez, S.; Botifoll, M.; Oksenberg, E.; Koch, C.; Borja, C.; Spadaro, M. C.; Giulio, V. D.; Ramasse, Q.; Abajo, F. J. G. de; Joselevich, E.; et al. Sub-Nanometer Mapping of Strain-Induced Band Structure Variations in Planar Nanowire Core-Shell Heterostructures. *Nat. Commun.* **2022**, *13*, 4089.
(37) Deitz, J. I.; Karki, S.; Marsillac, S. X.; Grassman, T. J.; McComb, D. W. Bandgap Profiling in CIGS Solar Cells via Valence Electron Energy-Loss Spectroscopy. *J. Appl. Phys.* **2018**, *123*, 115703.
(38) Zhan, W; Granerød, C S; Venkatachalapathy, V; Johansen, K M H; Jensen, I J T; Kuznetsov, A Y.; Prytz, Ø Nanoscale Mapping of Optical Band Gaps Using Monochromated Electron Energy Loss Spectroscopy. *Nanotechnology* **2017**, *28*, 105703.
(39) Crozier, P. A. Vibrational and Valence Aloof Beam EELS: A Potential Tool for Nondestructive Characterization of Nanoparticle Surfaces. *Ultramicroscopy* **2017**, *180*, 104−114.
(40) Gadre, C. A.; Yan, X.; Song, Q.; Li, J.; Gu, L.; Huyan, H.; Aoki, T.; Lee, S.-W.; Chen, G.; Wu, R.; et al. Nanoscale Imaging of Phonon Dynamics by Electron Microscopy. *Nature* **2022**, *606*, 292−297.
(41) Egoavil, R.; Gauquelin, N.; Martinez, G. T.; Aert, S. V.; Tendeloo, G. V.; Verbeeck, J. Atomic Resolution Mapping of Phonon Excitations in STEM-EELS Experiments. *Ultramicroscopy* **2014**, *147*, 1−7.

https://doi.org/10.1021/acs.jpcc.3c00572
J. Phys. Chem. C 2023, 127, 7762−7771

(42) Erni, R.; Browning, N. D. Quantification of the Size-Dependent Energy Gap of Individual CdSe Quantum Dots by Valence Electron Energy-Loss Spectroscopy. *Ultramicroscopy* **2007**, *107*, 267−273.
(43) Logar, M.; Xu, S.; Acharya, S.; Prinz, F. B. Variation of Energy Density of States in Quantum Dot Arrays Due to Interparticle Electronic Coupling. *Nano Lett.* **2015**, *15*, 1855−1860.
(44) Eljarrat, A.; López-Conesa, L.; López-Vidrier, J.; Hernández, S.; Garrido, B.; Magén, C.; Peiró, F.; Estradé, S. Retrieving the Electronic Properties of Silicon Nanocrystals Embedded in a Dielectric Matrix by Low-Loss EELS. *Nanoscale* **2014**, *6*, 14971−14983.
(45) Egerton, R. F. Vibrational-Loss EELS and the Avoidance of Radiation Damage. *Ultramicroscopy* **2015**, *159*, 95−100.
(46) Egerton, R. F.; Watanabe, M. Spatial Resolution in Transmission Electron Microscopy. *Micron* **2022**, *160*, No. 103304.
(47) Chuang, C.-H.; Lu, Y.-G.; Lee, K.; Ciston, J.; Dukovic, G. Strong Visible Absorption and Broad Time Scale Excited-State Relaxation in $(Ga_{1-x}Zn_x)(N_{1-x}O_x)$ Nanocrystals. *J. Am. Chem. Soc.* **2015**, *137*, 6452−6455.
(48) Huda, M. N.; Yan, Y.; Wei, S.-H.; Al-Jassim, M. M. Electronic Structure of ZnO:GaN Compounds: Asymmetric Bandgap Engineering. *Phys. Rev. B* **2008**, *78*, No. 195204.

https://doi.org/10.1021/acs.jpcc.3c00572
J. Phys. Chem. C 2023, 127, 7762−7771